Journal of
Synchrotron Radiation

ISSN 0909-0495

Received 16 April 2005
Accepted 30 June 2005

A beamline for high-pressure studies at the Advanced Light Source with a superconducting bending magnet as the source

Martin Kunz,[a,b]* Alastair A. MacDowell,[a] Wendel A. Caldwell,[a,b] Daniella Cambie,[a] Richard S. Celestre,[a] Edward E. Domning,[a] Robert M. Duarte,[a] Arianna E. Gleason,[a,b] James M. Glossinger,[a] Nicholas Kelez,[a] David W. Plate,[a] Tony Yu,[c] Joeseph M. Zaug,[c] Howard A. Padmore,[a] Raymond Jeanloz,[b] A. Paul Alivisatos[d] and Simon M. Clark[a]

[a]Lawrence Berkeley National Laboratory, 1 Cyclotron Road, Berkeley, CA 94720, USA, [b]Department of Earth and Planetary Sciences, University of California, Berkeley, CA 94720, USA, [c]Lawrence Livermore National Laboratory, 7000 East Avenue, Livermore, CA 94550, USA, and [d]Department of Chemistry, University of California, Berkeley, CA 94720, USA.
E-mail: mkunz@lbl.gov

A new facility for high-pressure diffraction and spectroscopy using diamond anvil high-pressure cells has been built at the Advanced Light Source on beamline 12.2.2. This beamline benefits from the hard X-radiation generated by a 6 T superconducting bending magnet (superbend). Useful X-ray flux is available between 5 keV and 35 keV. The radiation is transferred from the superbend to the experimental enclosure by the brightness-preserving optics of the beamline. These optics are comprised of a plane parabola collimating mirror, followed by a Kohzu monochromator vessel with Si(111) crystals ($E/\Delta E \simeq 7000$) and W/B_4C multilayers ($E/\Delta E \simeq 100$), and then a toroidal focusing mirror with variable focusing distance. The experimental enclosure contains an automated beam-positioning system, a set of slits, ion chambers, the sample positioning goniometry and area detector (CCD or image-plate detector). Future developments aim at the installation of a second endstation dedicated to *in situ* laser heating and a dedicated high-pressure single-crystal station, applying both monochromatic and polychromatic techniques.

Keywords: X-ray beamline; high pressure; X-ray diffraction; superbend; diamond anvil cell.

1. Introduction

The Advanced Light Source (ALS) is a relatively low-energy (1.9 GeV) third-generation synchrotron optimized for the production of VUV and soft X-ray light from undulators. However, local demand required the development of hard X-ray sources at the facility. As a result, three 6 T superconducting bending magnets replaced three 1.2 T warm bending magnets (Robin *et al.*, 2002; Tamura & Robinson, 2002). This resulted in a shift in the critical wavelength for these three sources from 3 keV to 12 keV allowing for the development of various hard X-ray programs. The protein crystallography (PX) community were the first group to capitalize on the new hard X-ray source (Trame *et al.*, 2004; MacDowell *et al.*, 2004). The local high-pressure community has now followed in the installation of a dedicated beamline for high-pressure experiments. The aim of this project is to offer a state-of-the-art user facility allowing X-ray diffraction, as well as EXAFS and X-ray imaging through a diamond anvil cell (DAC) at energies up to at least 35 keV, to the high-pressure community, specifically of the North American west coast. It constitutes a central component within a high-pressure science center, which ultimately will not only offer combined high-pressure/high-temperature *in situ* X-ray experiments but also a range of optical techniques such as Raman spectroscopy and Brillouin scattering. This paper describes the layout and characteristics of the high-pressure beamline and its first endstation, as well as some benchmarks relevant to X-ray diffraction experiments.

2. Source

The three 6 T superconducting bending magnets have been operating continuously since their installation in the ring lattice in 2002. They have been transparent to the users and can be viewed as a technical success, allowing low-energy rings to have access to an inexpensive hard X-ray bending-magnet source and the development of the associated hard X-ray

programs. The design allows for four beamlines per magnet, with inboard and outboard pairs of tangent points at field strengths of 4.37 and 5.29 T, respectively. These fields increased the critical energy from 3 keV for a 1.27 T normal conducting magnet to 10.5 and 12.7 keV, respectively. The high-pressure beamline described in this work has a source critical energy of 12.7 keV. The beam size in the ALS is small, owing to the small emittance of the beam [6.75 nm rad (horizontal, h), 0.15 nm rad (vertical, v)] and the small β functions [0.95 m (h), 1.5 m (v)]. Together with the small dispersion at the dipole position (dispersion = 0.57 m; slope of dispersion = −0.04), this yields 1σ electron beam sizes of 98 µm (h) × 15 µm (v).

3. Beamline design

Compared with the prototype ALS superconducting bending-magnet beamlines, which were optimized for the PX community (Trame *et al.*, 2004; MacDowell *et al.*, 2004), the design of the high-pressure beamline had to take into account the additional requirement of an extended energy range from the original 6–16 keV of the PX lines to at least 35 keV. The highest flux had to be concentrated on a 100 µm-diameter pinhole at the sample position with a 2 mrad horizontal convergence angle. The beamline is also required to scan in energy and be able to carry out extended X-ray absorption fine structure (EXAFS) type experiments as well as X-ray imaging techniques. Stable performance and rapid beam optimization were very important design considerations.

The beamline design is shown schematically in Fig. 1. It consists of the source, a vertically deflecting plane parabolic collimating mirror [grazing angle = 2.0 mrad, acceptance = 1.0 mrad (h) × 0.22 mrad (v)], M1, that provides parallel radiation in the vertical for a double-crystal monochromator (two flat crystals or two flat multilayers), followed by a toroidal focusing mirror, M2, the sample and backstop. For this beamline (ALS nomenclature 12.2.2) the various distances of the beamline components from the source are 6.5, 16.5, 18.8 and 28.2 m for the plane parabola, monochromator, toroid and sample, respectively (Fig. 1). This optical arrangement uses the toroid in the 2:1 horizontal demagnification with the result that astigmatic coma is eliminated (MacDowell *et al.*, 2004) and a focus spot of high fidelity is achieved. Ray-tracing using *Shadow* (Lai & Cerrina, 1986) indicated a focus spot size of 153 µm × 64 µm full width half-maximum (FWHM) with a beamline acceptance angle of 1.0 mrad (h) × 0.22 mrad (v) and a source size of 220 µm × 30 µm FWHM. The ray-trace has perfect optics of zero slope error. Real optics are imperfect with slope errors which will degrade the spot size. To achieve a spot size of 150 µm (h) × 100 µm (v) FWHM requires optical slope error tolerances of <1 µrad (MacDowell *et al.*, 2004). Such tolerances require very high quality optics near the limit of the current manufacturing capability.

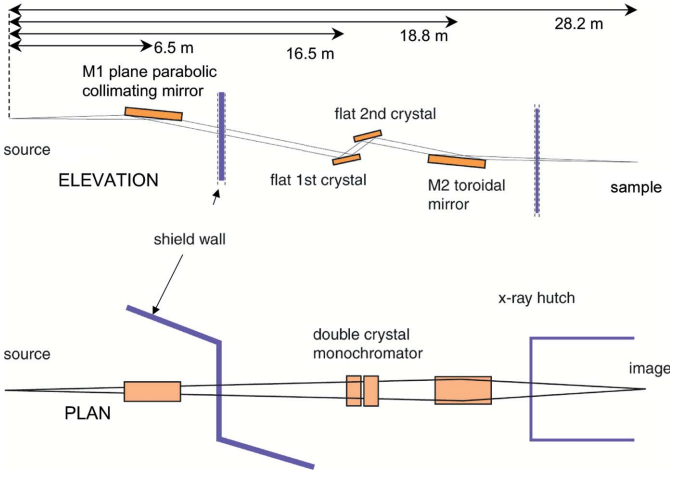

Figure 1
Schematic layout of the new high-pressure beamline with a superbend dipole magnet source. The beamline acceptance is 1.0 mrad (h) × 0.22 mrad (v). The toroidal M2 mirror demagnifies in the horizontal in a 2:1 ratio.

3.1. Optics

The description of the individual optics is as follows. The M1 plane parabola is a flat side-cooled silicon mirror assembled into a mechanical bender. Cooling was achieved using water-cooled copper bars held along the mirror sides with a 50–100 µm gap filled with gallium–indium–tin eutectic liquid metal. The parabolic shape of the M1 mirror was set using the ALS Long Trace Profiler (Irick, 1994). Metrology measurements indicated a slope error of 0.7 µrad r.m.s. and a finish of 0.25 nm r.m.s.

Following the pre-mirror is a standard APM Kohzu monochromator with custom in-house additions for the crystals and multilayer optics. Fig. 2 shows the schematic layout. The basic monochromator rotates all optics about the central axis that runs along the surface of the first crystal. This rotation is the main θ drive that determines the monochromator angle and thus X-ray energy selected. The first crystal is fixed to this main rotation platform, whilst the second crystal is mounted off a stack of four stages that in turn is supported from the main θ rotation platform. The four stages that the second crystal rides on can be adjusted to maintain the constant beam height offset required for the beamline optics.

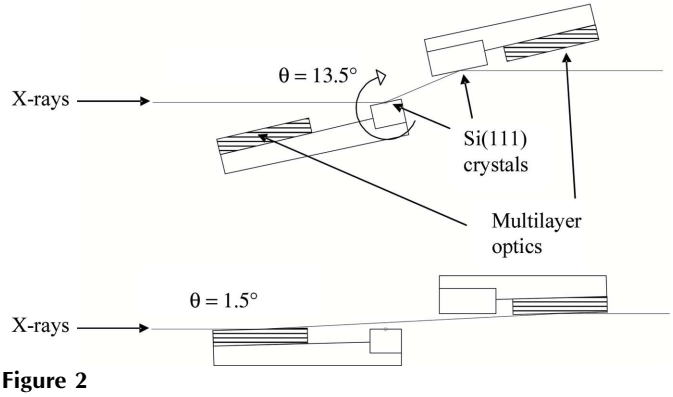

Figure 2
Schematic layout of the monochromator elements within the Kohzu monochromator.

The first multilayer is fixed to the first crystal support structure and, as shown in Fig. 2, is mounted upstream of the first crystal. The second multilayer is mounted on the stack of four stages along with the second Si(111) crystal. By rotating the main θ drive to the low grazing angle required for the multilayer, the off-axis location allows it to intercept the beam before the Si(111) crystal and directs the X-rays to the second multilayer (see Fig. 2). Of course the off-axis location of the first multilayer means that the X-rays will walk off the surface, but by suitable choice of mirror length (176 mm) and *d*-spacing (2.0 nm) it is possible to achieve a useful energy range of $\sim$14–29 keV before the beam has walked too far off the mirrors. The multilayers used were 150 layer pairs of W/B_4C supplied by Osmic with figure error <1 µrad r.m.s.

The maximum absorbed power density on the multilayer mirrors at 18 keV is calculated to be 1.65 W cm^{-2}. Finite-element analysis indicated that side cooling of the first multilayer optic would be adequate to retain the figure error of <1 µrad r.m.s. Side cooling was achieved by clamping water-cooled copper plates to both sides of the mirror with a gallium–indium–tin eutectic thermal interface.

For the flat Si(111) crystal the power load is 46 W with a maximum power density of 15.2 W cm^{-2} at 12.4 keV. At these power levels, internal water-cooling is adequate, but care has to be taken with the design of the water channels. A design similar to that used before was employed (MacDowell *et al.*, 2004), but the increased high energy of this beamline compared with the PX beamline precluded the use of epoxy for attaching the invar water plenums to the silicon crystal, as calculations (Howells, 1999) indicated that the epoxy lifetime would be less than one year. A low-temperature solder procedure was developed to attach the water plenums to the crystals. The thermal expansion of the silicon and invar are slightly different (2.0 ppm K^{-1} and 0.5 ppm K^{-1}, respectively), so we minimize the strain introduced by the temperature excursion during the soldering process by simply lowering the soldering liquidus temperature. The procedure was as follows. The sides of the silicon crystal and mating surface of the invar water plenum were lapped flat and then coated with 100 nm of gold by evaporation with a 5 nm chromium underlayer. The chosen solder consisted of 57% bismuth, 26% indium and 17% tin (type number 122801) from Indium Corporation of America selected for its low melting temperature of 351 K. The pieces were assembled at 363−373 K on a hot plate and worked with an ultrasonic soldering iron to help break up oxide layers and ensure a reliable mechanical solder seal. Subsequent rocking-curve measurements during beamline commissioning did not indicate that crystal strain was a problem for the Si(111) rocking-curve widths.

The second silicon crystal and multilayer optics have the shape of a rectangular parallelepiped ('brick'). The last optic is a silicon cylinder supplied by Seso and bent into a toroid by a mechanical bender. Slope errors on this unbent optic were measured as 1.4 µrad r.m.s. and a roughness of <0.4 nm r.m.s. Both the M1 and M2 mirrors were bent with cantilever-style spring bending mechanisms (Howells *et al.*, 2000).

The coating of the M1 mirror was 8 nm rhodium over 25 nm platinum over a 5 nm chromium 'glue' layer. A similar coating was used for the M2 mirror except that the rhodium coating was 4 nm thick rather than 8 nm thick. The reflectivity of the two different coatings along with the reflectivity of rhodium and platinum for a grazing angle of 2 mrad is shown in Fig. 3. The single platinum coating produces good reflectivity to high energy but has contaminating *L* edges in the 11–14 keV range. The use of a rhodium over platinum bilayer mirror allows for suppression of the platinum *L* edges as these low-energy X-rays are reflected from the rhodium layer. However, the high-energy X-rays penetrate the rhodium and are reflected from the underlying platinum layer. Thus this bilayer has a higher cut-off energy when compared with just a rhodium mirror at the same grazing angle. Fig. 2 suggests that the energy range is extended by $\sim$5 keV compared with a single rhodium layer. The reason for the difference in coating of the two mirrors is historical, as the M1 mirrors were supplied as a batch for the superbend protein crystallography project (MacDowell *et al.*, 2004). For this project the 8 nm rhodium thickness was more appropriate for the higher grazing angle of 4.5 mrad. For the more grazing angle of 2 mrad that is required for this high-pressure beamline, the thinner 4 nm rhodium layer was more appropriate, but not to the extent of recoating the M1 mirror.

3.2. Beam-position feedback scheme

The focused spot size at the sample is comparable with the sample size, which is typically less than the 150 µm inside diameter of the metal gasket in the DAC. Beamlines typically suffer from slow thermal variations of the beamline components, beam drifts and other unspecified environmental drifts that cause fluctuations in intensity and beam position at the sample. The requirement is for the beam to remain stable on the same position on the sample for at least the time it takes to record the required data. To solve the drift problems, we initially adopted a feedback system based on the horizontal

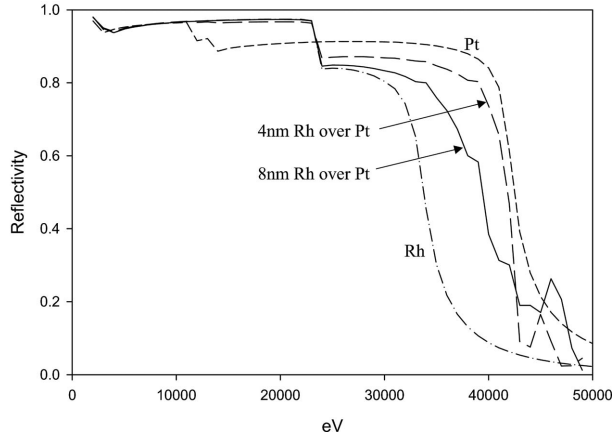

Figure 3
Calculated reflectivity plots of platinum, rhodium and two bilayers consisting of either 4 nm or 8 nm rhodium over 25 nm platinum. Zero angstrom roughness is assumed. The bilayer extends the energy-range cut-off beyond that for a simple rhodium mirror whilst reducing the effects of the platinum *L* absorption edges.

and vertical positional information from a fluorescence detector equipped with four PIN diodes that give beam positional information (Alkire *et al.*, 2000). The detector is located 70 cm before the focus position. This detector proved to have a non-linear response with photon energy, leading it to give an erroneous signal on which to provide beam-position feedback. The source of this non-linear response is still under investigation but initial work suggests that the signal level (typically <0.1 nA at 12 keV) is rather small compared with the noise and electronic drift levels and this poor signal-to-noise ratio is an inherent problem for this device in this beamline.

An alternative feedback scheme was used (MacDowell *et al.*, 2004). A cerium-doped yttrium aluminium garnet (YAG) scintillator is glued to the shutter blade of the CCD shutter (nm-Laser) located 50 cm before the sample. The scintillated beam image of the beam is viewed with a TV camera. This image is fed to a frame grabber that determines the beam-position parameters at 5 Hz. Vertical beam position is affected by movement of the M2 tilt, and horizontal beam position changes by rolling the second monochromator crystal. Beam-position centroid stabilities of ± 5 µm are typically achieved. The drawback of this control system is that it is only operational when the X-ray shutter is closed. When the shutter is open, the system operates in open-loop mode. However, the beamline has proved to be stable to the level of $\sim$20 µm over the typical longer recording times of $\sim$5 min. The beamline has proved to be more stable in this open-loop mode compared with the PX beamlines. It is surmised that the reduced power loading on the M1 mirror for the high-pressure beamline owing to the 2.0 mrad grazing angle helps with overall beamline stability compared with the PX beamlines which operate at a 4.5 mrad grazing angle. In order also to provide beam stabilization during longer (>5 min) exposure cycles, we adopted a combined scheme using the YAG scintillator as well as the fluorescence foil. The YAG scintillator is the dominant stabilizer. Whenever the shutter is closed, *i.e.* the YAG scintillator is brought into the beam, the beam is returned to its stored optimal position. When opening the shutter, the system records the current fluorescence values and keeps these constant as long as the shutter remains open. This procedure works fine for monochromatic diffraction experiments where the wavelength is fixed.

3.3. Endstation

In order to cover the expected range of experimental flexibility, two endstations are installed on a 3.6 m × 1.2 m optical table, which in turn is placed within a spacious (5.4 m × 3.2 m) hutch. After entering the hutch, the beam is conditioned and controlled by a set of absorption foils, a fast shutter, a set of horizontal and vertical aperture slits and a clean-up pinhole. The absorption foils (Cu, Zn, Pd, Sn, Ag and Mo), purchased from EXAFS-Materials, can be used for intensity attenuation at various energies and to calibrate the monochromator. This is routinely performed at the beginning of a new experiment, although tests during commissioning have shown the energy to be stable within 2 eV over the period of weeks of frequent energy changes. The fast shutter is water cooled and interfaced with the area detectors. A YAG scintillating crystal mounted on the front of the fast shutter allows for beam-position stabilization (see above). The slits and clean-up pinhole allow the beam to be shaped to the desired size. A clean circular beamspot is important for high-pressure experiments where even the smallest amount of X-rays falling on the highly scattering steel or rhenium gasket material can create intense background signals. Centering a 100 µm gasket hole onto a 100 µm beam requires an easy and fast pre-centering procedure. We solved this by using a mirror prism assembly (Fig. 4) mounted on a drive holding several pre-aligned tantalum pinholes. A parallax-free image of the DAC is viewed *via* a video camera. A small hole in the center of the mirror prism ensures unattenuated X-ray transmission without reducing the quality of the optical image. The DAC is moved to the pre-aligned beam-position center and then the mirror prism is moved out of the beam and replaced by a pre-aligned Ta pinhole acting as a scatter guard (Fig. 4).

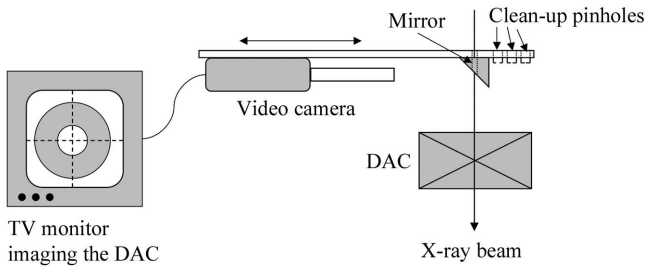

Figure 4
Schematic layout of the on-axis sample-viewing system and the scatter clean-up pinholes.

Of the two planned endstations, the first one has been commissioned and tested. Its present design is laid out for high-pressure powder diffraction in a DAC, mostly aiming at measuring accurate cell parameters to determine equations of state of solid (and liquid) material. Samples are mounted in a DAC onto a simple goniometer. The goniometer consists of, from bottom to top, the following stages (Fig. 5): 1, a horizontal translation stage perpendicular to the X-ray beam (*x*-direction); 2, a rotation stage with its axis vertical; 3, a vertical stage (*y*-direction); 4, a second horizontal-translation stage perpendicular to the beam (*x*-direction); 5, a horizontal-translation stage parallel to the beam (*z*-direction). This arrangement enables (*a*) centering the vertical rotation axis onto the beam using stage 1, and (*b*) placing the sample onto the rotation axis and beam using stages 4 and 5. This scheme allows the rotation axis to be used as a reference position relative to the detector plane, and thus to precisely determine the sample-to-detector distance (STD). Knowing this distance accurately is crucial for powder diffraction experiments, since the relative error in *d*-spacings (and thus cell parameters), $\Delta d/d$, scales linearly with the relative error in distance. Thus to achieve a desired accuracy of $\Delta d/d = 10^{-4}$ at a distance of 100 mm, the STD needs to be known to better than 10 µm. To determine the STD, we first place a calibrant (*e.g.* LaB_6, Si,

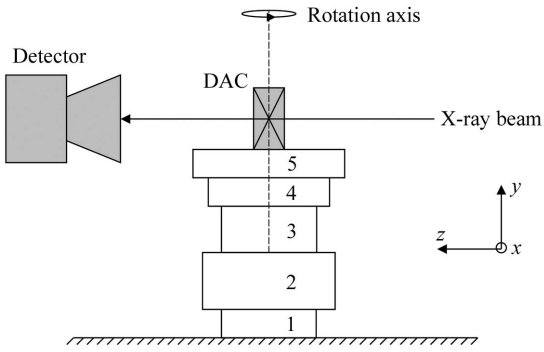

Figure 5
Schematic drawing of the sample stage on endstation 1. 1, *x*-translation stage to center the rotation axis on the beam; 2, rotation stage; 3, *y*-stage for vertical alignment; 4, *x*-stage to place the DAC center on the rotation axis and beam; 5, *z*-stage to place DAC center on rotation axis. The rotation axis is the reference position, which defines the distance to the detector. Once aligned onto the beam, its position remains fixed.

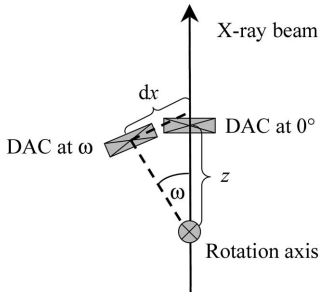

Figure 6
Schematic drawing of the sample-centering procedure. The aim is to place the DAC exactly onto the rotation axis. To do this we need to find the offset shift z. By measuring the DAC position at 0° and ω rotation relative to the X-ray beam (through scans of the sample hole across the beam), distance dx is determined. The offset z is then calculated as $z = \mathrm{d}x/\tan\omega$. Moving the DAC by this amount along the z-stage will place it on the rotation axis. The same procedure can also be used to place a calibrant onto the rotation axis, which is used to determine the distance between rotation axis and detector plane.

NaCl) onto the rotation axis and record a diffraction pattern. The known lattice parameter of the calibrant, together with the independently determined wavelength (by absorption edge, see above), allows us to determine the distance between the detector plane and the rotation axis from the diffraction pattern of the calibration material. This distance will then correspond to the STD if the DAC with sample is placed on the rotation axis as well. In order to center the calibrant and DAC onto the rotation axis, the absorption profile of the gasket hole containing the sample is scanned along the sample x-stage (4 in Fig. 5) across the X-ray beam at two different rotation angles. The shift of the gasket hole along the x-stage (dx) owing to the rotation divided by the rotation angle ($\tan\omega$) gives the offset of the sample from the rotation axis parallel to the beam (z) as $z = \mathrm{d}x/\tan\omega$ (Fig. 6). With this approach, samples can be placed onto the rotation axis of endstation 1 with a reproducibility of better than 8 μm.

A Mar345 image-plate detector (circular active area of 345 mm diameter, readout time $\simeq$ 40 s) or a Bruker Smart CCD (square active area of 100 mm edge length, readout time $\simeq$ 1 s) are used for detectors. Users tend to prefer the larger-sized slower image-plate reader over the smaller and faster CCD detector despite the reduced flexibility in STD. The instrumental resolution of the endstation depends on the divergence of the incident X-rays, size of the beam, thickness of the sample, diffraction angle, STD and point-spread function of the detector. Assuming a point-spread function of $\sim$0.25 mm for the CCD detector and a divergence of 0.5 mrad, we calculate a theoretical FWHM of 0.15° at 100 mm STD, which compares well with the observed value of 0.16°.

4. Beamline performance

The size of the collimated beam was measured by scanning a single blade of the slit assembly across the optimized beam. Beamline acceptance was 1.0 mrad (h) × 0.22 mrad (v). The measured size of 115 μm × 78 μm FWHM compares with the ray-traced theoretical value of 153 μm × 64 μm. The slightly larger spot size in the vertical can be attributed to the various summation of figure errors of the optics. The smaller size in the horizontal is less easy to explain. The current optical scheme is designed to eliminate astigmatic coma (MacDowell *et al.*, 2004) and so minimize the vertical beam size. Small changes in the grazing angles of M1 and M2 break this condition allowing for other aberrations to balance off against each other. Preliminary ray-tracing work has shown that there are slight improvements in the horizontal focused size by doing this.

The calculated and measured fluxes arriving at the sample with and without a pinhole collimator are shown in Fig. 7. The electron source used has an energy of 1.9 GeV within a field of 5.27 T at the tangent point. The absolute flux was measured by using an ion chamber (IC). The IC has a total length of 17 cm, an active length of 14.7 cm (guard electrodes occupied the 1.15 cm end sections) and is filled with 10^5 Pa of Ar gas. For measurements of the multilayer flux, 3.2 mm Al foils were inserted into the beam in order to avoid saturation of the IC. The current measured in the ion chamber is converted into a number of X-ray photons using a conversion factor of 26 eV of energy per electron–ion pair (Thompson, 2001). The photon flux derived from the ion chamber is checked against a silicon photodiode detector signal, which in turn was calibrated against a [NaI(Tl)] scintillator/photomultiplier-tube pulse-counting detector (Bicron model 1XMP.040B) operating at $<10^5$ Hz. The low rate of the scintillator detector allows for the assumption of zero dead time and thus linear response. The scintillator detection efficiency is considered to be 1.0 (Holl *et al.*, 1988).[1] The result of the flux measurements is compared

[1] This paper indicates that the visible photon yield from a NaI(Tl) scintillator is 38 photons keV^{-1} when irradiated with X-rays. We assume a conservative light coupling of these photons into the photomultiplier tube of $\sim$50%. The efficiency of the Hamamatsu R580 photomultiplier tube is $\sim$25% (http://usa.hamamatsu.com) at the emission wavelength of NaI(Tl), 430 nm. 12 keV X-rays are expected to generate $\sim$57 electrons per X-ray from the photocathode before entering the electron multiplier section. The scintillator photomultiplier combination is thus expected to single count X-rays with a quantum efficiency of 1.0 after absorption by the 125 μm-thick beryllium entrance window is taken into account.

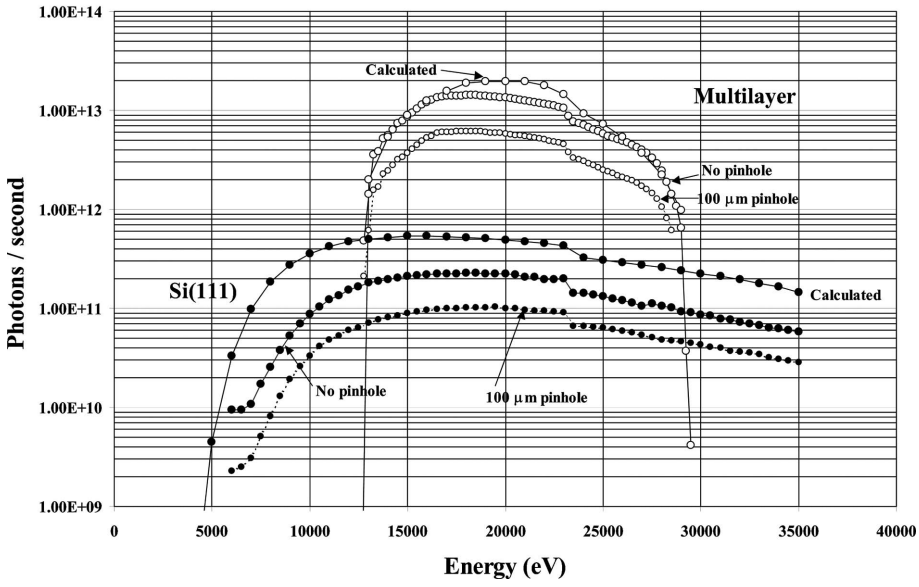

Figure 7
Calculated and measured total flux of the beamlines at the sample position. Flux rates are for 400 mA in the ALS and full acceptance of the beamline resulting in a convergence onto the sample of 2.0 mrad (h) × 0.15 mrad (v).

with the expected values in Fig. 7. The calculated total flux from the Si(111) crystals (no pinhole) is about twice the value measured. The reason for this discrepancy is still under investigation. With the insertion of a 100 μm pinhole the flux drops to 44% of the no-pinhole condition. Ray-tracing indicates that the flux reduction should be 36%. The smaller discrepancy between the flux measured and calculated through the pinhole is associated with the smaller spot size observed compared with the ray-traced version (see above). At high energies the flux is increasingly difficult to measure owing to the decreasing efficiency of both the ion-chamber and silicon-diode detectors. The flux plots thus terminate at 35 keV, and no roll-off owing to exceeding the critical angles of the mirrors is observed. The critical angle of the beamline is therefore slightly higher, consistent with the reflectivity plots of Fig. 3. For the multilayer, we observe the calculated and measured flux to be similar (less than a factor of 1.5) over the multilayer range. The rapid drop off of flux at either end of its range is due to the beam walking off the multilayer mirrors with energy change. The energy resolution of the 150 layer multilayer monochromator was measured at the rhodium edge as $E/\Delta E = 120$.

Two benchmarks for experiments on endstation 1 were determined. (1) The correlation between pressure determined using spectroscopic methods as compared with an internal diffraction standard. This gives us an indication of the reliability of compressibility measurements on 12.2.2. (2) The integral uncertainty on refinable parameters of a Rietveld refinement (atomic coordinates). This gives us a benchmark on the best possible accuracy for structural measurements.

Benchmark 1: Pressure in a DAC can be determined by measuring the pressure-induced shift of the laser-excited fluorescence line of a ruby grain within the pressure chamber (spectroscopic method) (*e.g.* Piermarini *et al.*, 1975). Alternatively, the known equation of state of a calibrant allows its diffraction signal to be used to deduce the pressure within a DAC (internal standard). Comparing the pressures derived from NaCl volumes against the ruby pressure gauge therefore gives us an indication on the reliability of compressibility data measured on endstation 1. To do this, a series of different ruby calibrations applied to our spectroscopic measurements (Piermarini *et al.*, 1975; Mao *et al.*, 1986; Holzapfel, 2003; Dorogokupets & Oganov, 2003) were compared with NaCl volumes measured on endstation 1 and converted into pressure using three different NaCl equations of state (Decker, 1971; Birch, 1986; Brown, 1999). NaCl powder together with eight different ruby grains were loaded into a Diacell membrane-driven DAC. Ethylcyclohexane (ECH) was used as a pressure medium. ECH was preferred to the usual ethanol–methanol mixture since many users are working with hygroscopic samples. The hydrostaticity of ECH is comparable with that of ethanol–methanol. Standard deviations for the spectroscopic data were determined from five to eight different measurements on different ruby grains. Volumes were calculated by fitting each of the first seven NaCl peaks individually using a Voigt function as implemented in *fit2d* (Hammersley, 1997) and converting each measurement into a volume. The seven volumes were used to calculate an average value and an estimated standard deviation. All measurements were performed at room temperature. The general agreement between the ruby scales and the NaCl pressure is good, which gives confidence in the capability of the beamline to produce reliable compressibility data. This is supported by a closer look at the data (Fig. 8): very good correspondence (mean deviation of 0.2 GPa) is observed for the equation of state given by Decker (1971) and the ruby scale proposed by Piermarini *et al.* (1975) (Fig. 8). Since the Piermarini scale is gauged solely against the Decker equation of state, these two scales should show identical pressures, provided the volumes extracted are reliable. The good agreement between these two scales found on our beamline confirms therefore the internal consistency of the NaCl compressibility measured on 12.2.2 endstation 1. Good agreement is also observed between Birch's equation of state and the ruby scale proposed by Mao *et al.* (1986), Holzapfel (2003) and Dorogokupets & Oganov (2003). All of these ruby scales were calibrated against the compressibility of a series of different metals. Brown's (1999) compressibility model seems to be in best agreement with Piermarini's ruby scale.

Benchmark 2. It is well known that estimated standard deviations (e.s.d.s) of atomic coordinates and cell parameters, derived analytically from Rietveld refinements, tend to be underestimated (*e.g.* Hill, 1991). In order to establish an

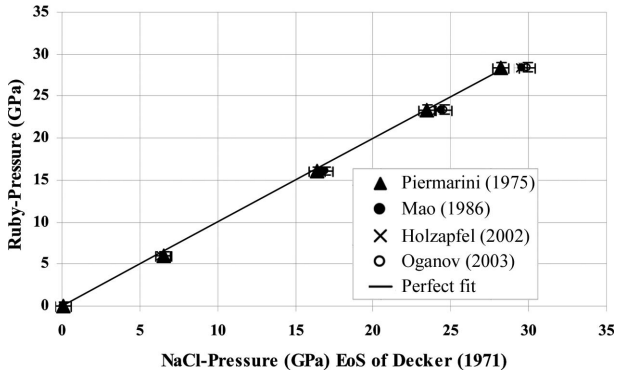

Figure 8
Comparison between pressures measured using the ruby fluorescence method with pressure determined with the help of NaCl as internal standard.

integral set of standard deviations for 12.2.2 endstation 1, a powder diffraction experiment on a standard (LaB_6) in air was repeated nine times including the subsequent data reduction and analysis with *fit2d* (Hammersley, 1997; Hammersley *et al.*, 1996) and *GSAS* (Larson & Von Dreele, 2000; Toby, 2001). LaB_6 was used since it is known to have very low strain broadening and is therefore used as a standard in powder diffraction (NIST standard 660a). The experiments were conducted at an energy of 25.514 keV (λ = 0.48593 Å). This specific energy was chosen since it corresponds to the Ag *K*-edge and therefore allowed for a precise wavelength calibration independent of the diffraction experiment. A Smart 6000 CCD (active area 10 cm × 10 cm, pixel size ~0.1 mm × 0.1 mm) was used as detector. Frames were corrected for dark current as well as spatial distortion using the Smart software. For each exposure, the sample (Sigma Aldrich 24,185-7, Lot # MU 04702MR) was loaded into a gasket hole of diameter 0.15 mm and mounted outside a DAC onto the goniometer. After each exposure the sample was taken off the beamline, re-mounted on its holder and placed back on the goniometer before applying the centering routines described above. Each of the resulting data sets was first used to determine a STD using the cell parameters given by the National Bureau of Standards (4.1569 Å) (NIST SRM 660a). The STD, which was used to convert the two-dimensional diffraction images into one-dimensional 2θ *versus* intensity plots, was taken from the average of these nine individual measurements (99.949 mm). For the Rietveld refinement in *GSAS*, lattice parameter, zero point, background parameters (shifted Chebyeshev with 12 parameters), peak profile parameters (six parameters of a pseudo Voigt function) as well as the X-coordinate of the B atom and an isotropic displacement parameter (U_{iso}) for La and B were refined. The results are summarized in Table 1. As can be seen, our diffraction system produces lattice parameters with an internal precision of 4×10^{-4}. This figure could be improved by a factor of two or three by using a larger detector at a longer STD. When comparing our refined cell parameter to the theoretical value published by NIST SRM-660a, we find a striking difference of 4.167 (2) Å *versus* 4.157 Å, *i.e.* about five times the estimated standard deviation.

Table 1
Refined values for cell parameter (a), isotropic displacement parameters (U_{iso}) and interatomic distance (La–B) from nine independent powder diffraction experiments on LaB_6 (NIST SMT 660*a*).

Number	a (Å)	U_{iso}(B) (Å^2)	U_{iso}(B) (Å^2)	La–B (Å)
1	4.167960	0.00418	0.00424	3.0495
2	4.163424	0.00563	0.00330	3.0454
3	4.167552	0.00598	0.00386	3.0448
4	4.168971	0.00209	0.00834	3.0420
5	4.168985	0.00138	0.00341	3.0474
6	4.168031	0.00302	0.00857	3.0479
7	4.167924	0.00279	0.00269	3.0532
8	4.165755	0.00274	0.00678	3.0500
9	4.167202	0.00214	0.00365	3.0680
Average	4.167 (1)	0.003 (2)	0.005 (2)	3.050 (8)

We attribute this discrepancy to a real discrepancy between our sample and the NIST sample. Such a discrepancy cannot be fully compensated in the distance calibration procedure since the effect of a different lattice parameter varies with $\sin\theta$, whereas the STD affects the peak position as a function of $\tan\theta$. A full profile refinement including a zero point will therefore reflect this discrepancy. Forcing the zero point to a value of zero was not an option because it prevented the Rietveld refinement from convergence owing to large positional mismatches at high angles. Inter-atomic distances are affected by both peak position and peak intensity. In our case, the La–B distance is determined by the lattice parameter on the one hand and a single free coordinate x(B) on the other. Here we find a precision of 2×10^{-3}. Despite the fact that we observe a larger cell parameter than the NIST value, our La–B distance [3.050 (7) Å] is within one e.s.d. of the NIST value (3.054 Å). Although it is very difficult to extract meaningful displacement parameters from Rietveld refinements, refined U_{iso} parameters can still give an indication of the quality of the intensity data. As shown in Table 1, all U_{iso} parameters refined to positive values, which are in a physically meaningful order of magnitude. This lends confidence in the measured intensities, although we do not aim at interpreting displacement parameters from high-pressure powder diffraction experiments.

5. Control system

The success of beamlines is becoming more dependent on their ease of use, which is strongly influenced by the control software. This high-pressure facility employs separate control systems for the beamline and endstation. The beamline is operated by a now standard ALS control system based on *Labview* (National Instruments). All hardware and software components are modular, because most beamlines contain a limited set of relatively standard components that are independent of the experimental endstation. This beamline control system can operate stand-alone and be used to commission the beamline without a functioning endstation. Following commissioning, the beamline control system can be put into a driven mode and receive control inputs *via* the local network from the endstation control system. Such commands can shift

the energy, control the beam convergence onto the sample and tune up the beamline.

The endstation control code is also an in-house control system based on *Labview*. However, the ever changing requirements of the experiments require continued modifications to the endstation control system. This takes significant effort if the procedure is to modify the endstation code each time a change is required. To address this issue the software is to have the higher level macro system developed on top of the current system that will allow users to modify the control as required for the separate experiments. This development is underway.

6. Future developments

The hutch was designed to be long enough to accommodate a second endstation. Slits at the location of the first station will act as a virtual source that will be re-imaged by KB mirrors with a demagnification of 2×6 (h $\times$ v) onto a second station. By adjusting the slits at the virtual (secondary) source, a spot size of $\sim$10 µm on the sample is expected. This upgrade is underway. The second station is to be equipped with a double-sided laser-heating system.

Once the laser-heating set-up is installed and commissioned, we plan to replace the powder diffraction set-up of endstation 1 with a single-crystal diffractometer. The photon flux and energy spectrum provided by a superconducting bending magnet provides an excellent source to interface DACs with single-crystal X-ray diffraction. This is not only of high interest for the local high-pressure community but is also in line with recent international developments in high-pressure crystallography. The quest for higher and higher pressures involves smaller and smaller sample volumes, which in turn results in poorer powder statistics, thus imposing an intrinsic pressure limit for powder crystallography. It can be shown that, in order to maintain a measured accuracy on powder diffraction intensities of 5%, the number of grains required is about 10^6. This in turn poses a limit on minimal sample volume and thus maximal pressure if one assumes a minimal acceptable grain size ($\sim$1 µm). In order to overcome this limitation, we plan to revitalize polychromatic single-crystal diffraction. We intend to develop a scanning monochromator technique in order to circumvent familiar problems of Laue diffraction (harmonic overlap, energy-specific absorption correction). Alternatively we also envisage exploiting the wide bandpass of the multilayer monochromator. This offers a pink beam, which may also be used to solve the above-mentioned problem of harmonic overlap. In any case, an approach using polychromatic single-crystal diffraction will facilitate the extraction of structural data from static samples and is thus ideal for combining with the presently installed laser-heating set-up.

7. Conclusions

Endstation 1 of beamline 12.2.2 of the Advanced Light Source offers an experimental facility dedicated to high-pressure research. Its energy range and flux permit X-ray powder diffraction and X-ray spectroscopic experiments between 5 and 35 keV up to pressures of >50 GPa and temperatures of 800 K. This demonstrates that, with state-of-the-art beamline technology, competitive high-pressure research can be conducted at a 1.9 GeV storage ring. Flux and energy range of this type of beamline are ideal for future developments in the rising field of synchrotron-based high-pressure single-crystal X-ray diffraction.

We would like to thank the many staff at the Lawrence Berkeley National Laboratory who have contributed to this project. We would also like to thank the many beamline users who have borne with us through all of the teething problems and who's suggestions have contributed greatly to the final configuration of this beamline. We would like to thank Tomas Diaz De La Rubia and Lou Terminello at the Lawrence Livermore National Laboratory for contributions of equipment that enabled us to complete and enhance endstation 1. The Advanced Light Source is supported by the Director, Office of Science, Office of Basic Energy Sciences, Materials Sciences Division, of the US Department of Energy under Contract No. DE-AC03-76SF00098 at Lawrence Berkeley National Laboratory and University of California, Berkeley, California. COMPRES, the Consortium for Materials Properties Research in Earth Sciences under NSF Cooperative Agreement EAR 01-35554 supported this project through funding of MK, WAC and AEG as well as crucial beamline equipment.

References

Alkire, R. W., Rosembaum, G. & Evans, G. (2000). *J. Synchrotron Rad.* **7**, 61–68.
Birch, F. (1986). *J. Geophys. Res.* **91**(B5), 4949–4954.
Brown, M. J. (1999). *J. Appl. Phys.* **86**, 5801–5808.
Decker, D. L. (1971). *J. Appl. Phys.* **42**, 3239–3244.
Dorogokupets, P. I. & Oganov, A. R. (2003). *Dokl. Earth Sci.* **391**A, 854–857.

Hammersley, A. P. (1997). ESRF Internal Report ESRF97HA02T. ESRF, Grenoble, France.
Hammersley, A. P., Svensson, S. O., Hanfland, M., Fitch, A. N. & Häusermann, D. (1996). *High Press. Res.* **14**, 235–248.
Hill, R. J. (1991). In *The Rietveld Method*, edited by R. A. Young. Oxford University Press.
Holl, I., Lorenz, E. & Mageras, G. (1988). *IEEE Trans. Nucl. Sci.* **35** 105–109.
Holzapfel, W. B. (2003). *J. Appl. Phys.* **93**, 1813–1818.
Howells, M. R. (1999). Advanced Light Source Note LSBL-529. ALS, Berkeley, USA.
Howells, M. R., Cambie, D., Duarte, R., Irick, S., MacDowell, A. A., Padmore, H. A., Renner, T., Seungyu, R. & Sandler, R. (2000). *Opt. Eng.* **39**, 2748–2762.
Irick, S. (1994). *Nucl. Instrum. Methods*, A**347**, 226–230.
Lai, B. & Cerrina, F. (1986). *Nucl. Instrum. Methods*, A**246**, 337–341.
Larson, A. C. & Von Dreele, R. B. (2000). *General Structure Analysis System (GSAS)*, Los Alamos National Laboratory Report LAUR 86–748. Los Alamos National Laboratory, NM, USA.
MacDowell, A. A., Celestre, R. S., Howells, M. R., McKinney, W., Krupnick, J., Cambie, D., Domning, E. E, Duarte, R. M., Kelez, N., Plate, D. W., Cork, C. W., Earnest, T. N., Dickert, J., Meigs, G., Ralston, C., Holton, J. M., Alber, T., Berger, J. M., Agard, D. A. & Padmore, H. A. (2004). *J. Synchrotron Rad.* **11**, 447–455.
Mao, H.-K., Xu, J. & Bell, P. M. (1986). *J. Geophys. Res. Solid Earth Planets*, **91**(B5), 4673–4676.
Piermarini, G. J., Block, S., Barnett, J. D. & Forman, R. A. (1975). *J. Appl. Phys.* **46**, 2774–2780.
Robin, D., Benjegerdes, R., Biocca, A., Bish, P., Brown, W., Calais, D., Chin, M., Corradi, C., Coulomb, D., De Vries, J., DeMarco, R., Fahmie, M., Geyer, A., Harkins, J., Henderson, T., Hinkson, J., Hoyer, E., Hull, D., Jacobson, S., Krupnick, J., Marks, S., McDonald, J., Mollinari, P., Mueller, R., Nadolski, L., Nishimura, K., Ottens, F., Paterson, J. A., Pipersky, P., Ritchie, A., Rossi, S., Salvant, B., Schlueter, R., Schwartz, A., Spring, J., Steier, C., Taylor, C., Thur, W., Timossi, C., Wandesforde, J. & Zbasnik, J. (2002). *Proceedings of the 2002 European Particle Accelerator Conference*, Paris, France, pp. 215–217. Geneva: EPAC.
Tamura, L. & Robinson, A. (2002). *Synchrotron Rad. News*, **15**, 30–34.
Thompson, A. C. (2001). *X-ray Data Booklet*, 2nd edition, edited by A. C. Thompson and D. Vaughan, pp. 4–35, LBNL/PUB-490 Revision 2. LBNL, Berkeley, CA, USA.
Toby, B. H. (2001). *J. Appl. Cryst.* **34**, 210–213.
Trame, C., MacDowell, A. A., Celestre, R. S., Padmore, H. A., Cambie, D., Domning, E. E., Duarte, R. M., Kelez, N., Plate, D. W., Holton, J. M., Frankel, K., Tsutakawa S., Tainer J. & Cooper, P. K. (2004). *AIP Conf Proc.* **705**, 502–505.